Single-Atom High-Temperature Catalysis on Rh_1O_5 Cluster for Production of Syngas from Methane

Yu Tang,[1¶] Victor Fung,[2¶] Xiaoyan Zhang,[1¶] Yuting Li,[1¶] Luan Nguyen,[1] Tomohiro Sakata,[3] Kotaro Higashi, [3] De-en Jiang*[2] and Franklin (Feng) Tao*[1]

[1]Department of Chemical and Petroleum Engineering, University of Kansas, Lawrence, KS, 66049, USA

[2]Department of Chemistry, University of California, Riverside, CA, 92521, USA

[3]Innovation Research Center for Fuel Cells and Graduate School of Informatics and Engineering, The University of Electro-Communications, Chofu, Tokyo, 182-8585, Japan

¶ These authors equally contributed to this work.

* Correspondence and requests for materials should be addressed to emails: franklin.tao.2017@gmail.com (F.T.) and djiang@ucr.edu (D.J.)

Abstract

Single-atom catalysts are a relatively new type of catalyst active for numerous reactions but mainly for chemical transformations performed at low or intermediate temperatures. Here we report that singly dispersed Rh_1O_5 clusters on TiO_2 can catalyze the partial oxidation of methane (POM) at high temperatures with a selectivity of 97% for producing syngas ($CO+H_2$) and high activity with a long catalytic durability at 650°C. The long durability results from the substitution of a Ti atom of TiO_2 surface lattice by Rh_1, which forms singly dispersed Rh_1 atom coordinating with five oxygen atoms (Rh_1O_5), an under-coordinated environment but with nearly saturated bonding with oxygen atoms. Computational studies show the back donation of electron from d_{z^2} orbital of the singly dispersed Rh_1 atom to unoccupied orbital of adsorbed CH_n ($n>1$) results in the charge depletion of the Rh_1 atom and a strong binding of CH_n to Rh_1. This strong binding decreases the barrier for activating C-H, thus leading to high activity of Rh_1/TiO_2. Cationic Rh_1 single atom anchored on TiO_2 exhibits a weak binding to atomic carbon in contrast to the strong binding of metallic Rh surface to atomic carbon. The weak binding of atomic carbon and the spatial isolation of Rh_1 on TiO_2 prevents atomic carbon from coupling on Rh_1/TiO_2 to form carbon layers, making Rh_1/TiO_2 resistant from carbon deposition supported metal catalysts for POM. The highly active, selective and durable high-temperature single-atom catalysis performed at 650°C demonstrates a avenue application of single-atom catalysis to chemical transformations at high temperatures.

Keywords: Single atom catalyst, syngas, partial oxidation, methane, rhodium, AP-XPS, in-situ, operando

Introduction

The production of synthesis gas (syngas) from methane has mainly been achieved through the catalytic steam reforming of methane (SRM) at 800°C or through noncatalytic homogeneous partial oxidation of methane (POM) at >1127°C.[1-4] Steam reforming of methane at >800°C has been the predominant catalytic process in the industrial production of syngas since the 1930s.[2-5] Supported Ni catalysts have been the main industrial catalysts for the steam reforming of methane which suffers from a serious issue of carbon deposition despite the fact that a significant number of catalysts of SRM were reported in literature.[2-4] Although the addition of more H_2O to the reactor is used to avoid coke formation in methane reforming, it unfortunately creates new problems in terms of increasing the H_2/CO ratio through the water-gas shift reaction. A high H_2/CO ratio consequently limits the direct use of the CO and H_2 mixture in downstream processes, mainly Fischer-Tropsch synthesis.[2-4] Meanwhile, the noncatalytic POM is a homogeneous reaction processed at an extremely high temperature (>1127°C), which consumes a significant amount of energy to maintain the reaction temperatures and thus results in a large carbon footprint and a need for the costly maintenance of the reactors.

The limitations of catalytic SRM and noncatalytic POM drove explorations into catalytic POM as early as the 1920s.[2-4] Compared to noncatalytic POM performed at >1127°C, catalytic POM can be performed at reaction temperatures lower than 1127°C, significantly reducing energy costs. Due to the mildly exothermic nature of POM at room temperature, performing POM at low temperatures is thermodynamically feasible as long as its kinetics can be promoted by a catalyst. Significant efforts in this area were made in the last few decades as reviewed in literature.[2,3,6-8] Ni supported on alumina were the main catalysts for POM studied in the 1920s-

1940s.[9,10] In the 1980s-1990s, Ni catalysts modified with different supports including Y_2O_3, Co_3O_4, ZrO_2, UO_2, ThO_2, and rare earth oxides were then reported.[2-4] The main problem of these Ni-based POM catalysts is the formation of whisker carbon which clogs reactors substantially.[11-17] In addition, by using $CaAl_2O_4$, $AlPO_4$-5, alkaline metal oxide-modified alumina, or $Ca_{0.8}Sr_{0.2}TiO_3$ as a support of Ni, the thermal stability of Ni-based catalysts was improved to some extent although the selectivity for producing CO and H_2 was sacrificed.[18-22] Unfortunately, the issues of deactivation of nickel catalysts by carbon deposition during POM remain unresolved so far.[2]

In the 1980s, Green et al. reported $Ln_2M_2O_7$ (Ln=La, Pr, Eu, La, Dy, Yb, Ba, Bi, and M=Ru, Ir, Pt, Rh) catalysts exhibiting high activity and selectivity which led to a renaissance in catalytic POM studies.[4,10,23,24] Their early reports on $Ln_2M_2O_7$ inspired a large number of studies on precious metals and related catalysts since the 1980s;[2] Pt, Pd and Rh with a loading of 0.5wt%-5.0wt% on different types of supports including alumina foam, mixed oxides were investigated for POM. Through these studies, an ordering of activity impacted by a support was suggested: $Y_2O_3 > La_2O_3 > MgO > Al_2O_3 > SiO_2$ and $Y_2O_3 > ZrO_2 > TiO_2$.[25] These supported noble metals are highly active for POM although their thermal stabilities were not reported in detail.[2] Different from these Ni-based and noble metal-based catalysts, molybdenum carbide was reported by York et al;[26-28] this type of catalysts has an activity similar to noble metals; however, it readily deactivates through a two-step process under reaction conditions, where molybdenum carbide is first oxidized to molybdenum oxide and then vaporization occurs at high temperatures under 1 atm pressure.[2,3,6,7,26-28] Despite these significant efforts in the development of different types of POM catalysts, these reported catalysts have still suffered from either carbon deposition and/or a loss or a harmful restructuring of the active catalyst components during POM.

The literature has demonstrated that single-atom catalysts of many transition metals including Pt, Pd and Rh exhibit distinctly different catalytic performances for a number of reactions at relatively low temperature.[29-39] Compared to the continuously packed metal atoms on the surface of a metal particle, a singly dispersed metal atom, or an isolated metal atom, anchored on surface of a nonmetallic support, typically an oxide, is in a distinctly different chemical and coordination environment and thus exhibits a very different electronic state. For instance, Rh atoms were anchored to the internal surface of a micropore of the aluminosilicate ZSM-5 through proton exchange, making single-atom catalysts, Rh_1@ZSM-5; these reported single-atom sites immobilized in the 0.56 nm wide micropores of ZSM-5 are active for synthesis of acetic acid and methanol through coupling of CH_4, CO and O_2 in the microporous reactor where reactant molecules are delivered through the diffusion of dissolved gas molecules in aqueous solution under a high pressure gas phase at low temperatures of ≤150ºC.[40,41] These singly dispersed metal atoms, or single atoms, on a nonmetallic surface are typically under-coordinated, either electronically deficient or rich, which offer them a high tendency to bind to a reactant molecule or intermediate. However, one major challenge of single-atom catalysts is their short durability at high catalysis temperature and low reusability as their singly dispersed single-atom sites readily sinter at elevated temperatures[42,3,43,44]. Thus, most single-atom catalysts function well at room temperature or a relatively low temperatures (≤300ºC) but not at high temperatures (≥450ºC), although a significant portion of chemical productions of chemical and petrochemical industries are performed at high temperatures driven by thermodynamics or/and kinetics. Notably, the high temperature defined here is different from that of high temperature processes in industries which run at 800ºC or higher.

Herein we report a high-temperature single-atom catalyst, Rh_1/TiO_2 which is highly

active for POM at 650ºC. During the high temperature catalysis at 650ºC, its Rh_1 atom coordinates with five O atoms, a nearly saturated coordination shell. This single-atom catalyst exhibits long durability and extraordinary catalytic performance at 650ºC for at least 240 hrs and high reusability from 20 repeat runs in the temperature range of 450-650ºC.

Results and Discussion

Catalytic performance of single-atom catalyst Rh_1/TiO_2

The single-atom catalyst, Rh_1/TiO_2 was prepared through a deposition precipitate method modified for the preparation of Rh_1/TiO_2. Rh(III) cations were introduced to surface of TiO_2 nanoparticles followed by drying at 60ºC in air overnight and then annealing at 650ºC in air for 4 hrs. Based on ICP-AES measurements, the actual loading of Rh on TiO_2 is 0.037wt%. Details of the preparation can be found in the section of Experimental Methods and Computational Approaches. For convenience, 0.037wt%Rh/TiO_2, Rh_1/TiO_2 and Rh_1O_5/TiO_2 are interchangeably used to refer the same catalyst in this article, depending on which piece of specific information (concentration, single dispersion, or coordination) of this catalyst is emphasized.

Compared to the inactive TiO_2 nanoparticles for POM in the temperature range of 300-700 ºC (Figure S1a), the Rh_1/TiO_2 catalyst is highly active for POM in the range of 450-650ºC under a flow of a mixture of 25 ml/min 10% CH_4 and 25 ml/min 5% O_2 (Figure S2). At 650 ºC, 50 mg of 0.037wt% Rh/TiO_2 has a conversion of 80% for CH_4 (Figure 1a). The selectivities for producing H_2 and CO at 650ºC are 96% and 98%, respectively (Figures 1b and 1c). This catalytic activity and selectivity on Rh_1/TiO_2 remain after over 240 hrs of

time on stream (Figure 1). There was no interphase diffusion limit since the conversion of CH_4 remained nearly the same while the flow rate of the mixture of CH_4 and O_2 varied in the range of 30-100 ml/min (Figure S3). The observed by-products are mainly CO_2 and H_2O which are formed from a competing reaction channel, the complete oxidation of methane; here the selectivities for forming by-products CO_2 and H_2O are 4% and 2%, respectively. In the kinetics-controlled regime, the Rh_1/TiO_2 catalyst exhibits an extraordinarily high turnover rate of 2428

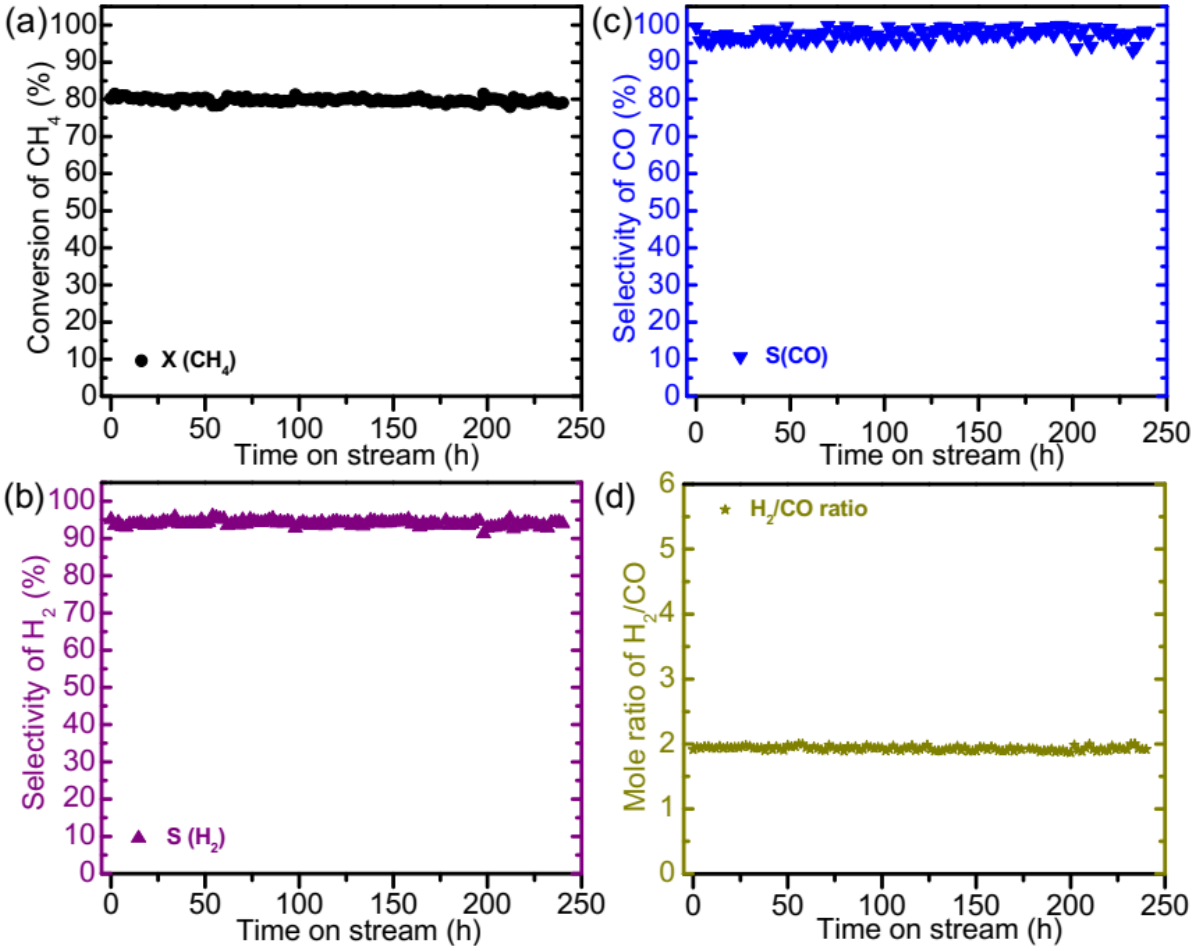

Figure 1. Catalytic durability of Rh_1/TiO_2 catalyst (0.037wt%Rh/TiO_2) for POM in a period of 10 days. (a) Conversion of CH_4 at 650°C; (b) Selectivity for producing H_2 at 650°C; (c) Selectivity for producing CO at 650°C; (d) H_2/CO molar ratio at 650°C. Catalysis conditions: catalyst is 50 mg 0.037wt%Rh/TiO_2; the gas fed to the reactor is a mixture of 25 mL/min of 10% CH_4 and 25 ml/min of 5% O_2; catalysis temperature is 650°C.

H_2 molecules produced from a Rh_1-based site per minute at 650°C. Details of calculation of

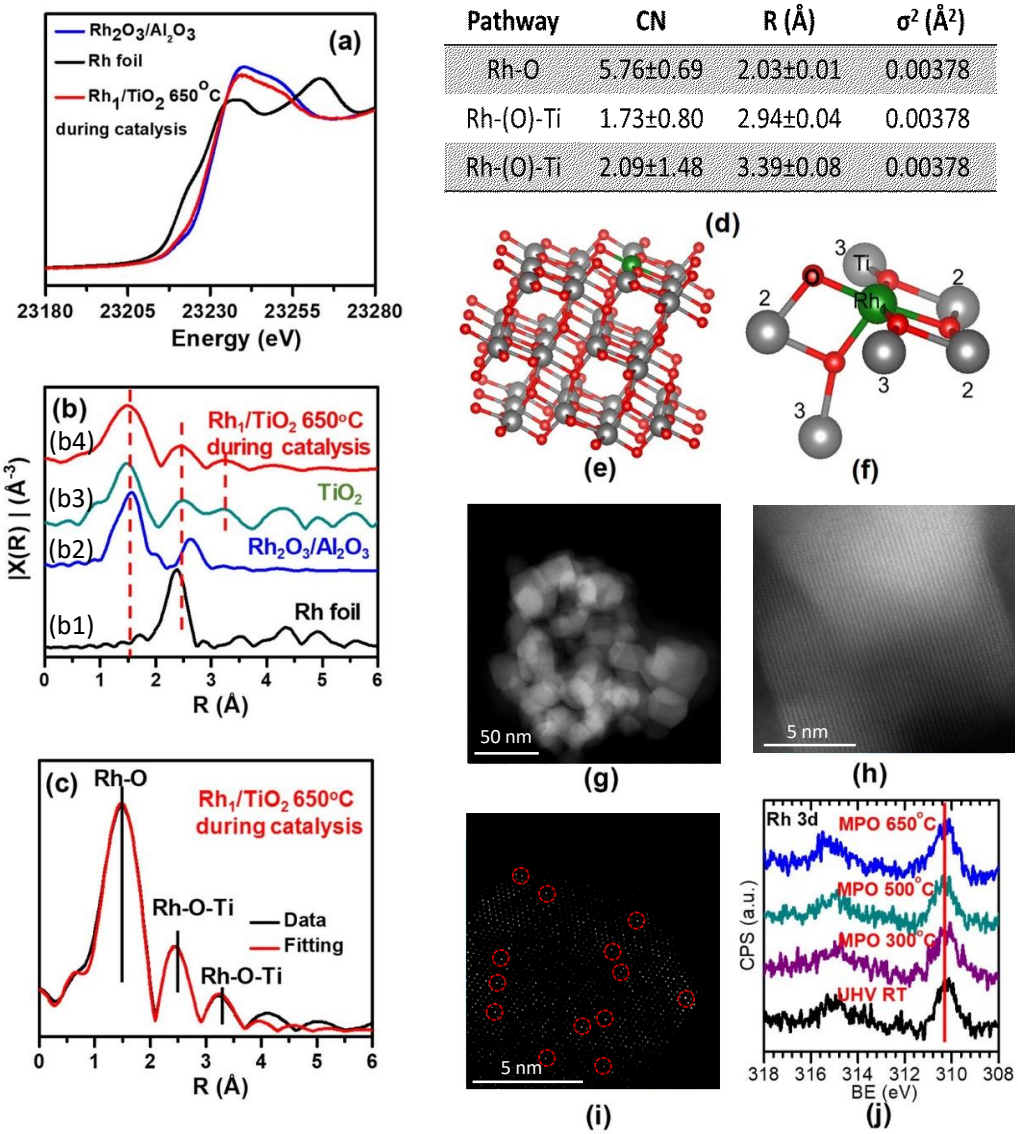

Figure 2. In-situ and operando studies of the 0.037wt%Rh/TiO_2 (Rh_1/TiO_2) catalyst for POM. (a-c) In-situ XANES and EXAFS studies of Rh K-edge. **(a)** XANES data of Rh foil, Rh_2O_3/Al_2O_3 and Rh_1/TiO_2 under catalytic condition of 650°C; (b) k^2-weighted Rh K-edge EXAFS data in *r* space of (b1) Rh foil collected in air, (b2) Rh_2O_3/Al_2O_3 collected in air, and (b4) Rh_1/TiO_2 collected in the flowing mixture of CH_4 and O_2 through in-situ study approach of EXAFS, and (b3) k^2-weighted Ti K-edge EXAFS data in *r* space of TiO_2 collected in air; **(c)** k^2-weighted Rh K-edge EXAFS data in *r* space of Rh_1/TiO_2 collected in the flowing mixture of CH_4 and O_2 through in-situ study approach of EXAFS (black line) and the fitted curve (red line). **(d)** List of fitting parameters including bond lengths and coordination number. **(e)** Optimized structural model of catalyst Rh_1/TiO_2. **(f)** Coordination environment of Rh_1 atoms in the optimized structural model of (e). **(g)** Large scale TEM image of catalyst particles after catalysis at 650°C for 240 hrs. **(h)** High resolution TEM image of a particle of (g); **(i)** High resolution aberration-corrected HAADF-STEM images visualizing singly dispersed Rh atoms anchored on TiO_2 marked in red circles. **(j)** AP-XPS spectra of Rh *3d* of Rh_1/TiO_2 in UHV at 25°C, in the mixture of CH_4 and O_2 at 300°C, 500°C and 650°C.

the TOR can be found in Section 7.2 of the supporting information (SI). The distinct difference

in catalytic activity between pure TiO_2 (Figure S1) and Rh_1/TiO_2 (Figure 1) clearly shows the crucial role of the anchored Rh_1 atom although the loading is as low as only 0.037wt%. To test the reusability of the catalyst, catalysis was performed from 300°C to 650°C on Rh_1/TiO_2, followed by cooling to 300°C before the next cycle. for a total of 20 cycles on Rh_1/TiO_2. Compared to the catalytic performance of the 1st cycle (Figure S2a), the decay in catalytic activity and selectivities at the 20th cycle (Figure S2b) is less than 4% over a period of about 360 hrs. This suggests quite a high reusability for Rh_1/TiO_2.

The single-atom catalyst Rh_1/TiO_2 also exhibited quite a long durability for POM at 650°C for at least 240 hrs. As shown in Figure 1a, the conversion of CH_4 (80%) remained without any decay at the 240th hr compared to the 0th hr. In addition, the selectivity for production of H_2 and CO remained at 96% and 98%, respectively, under 650°C for the whole duration with negligible changes (Figures 1b and 1c). The molar ratio of produced H_2/CO remained at 2.0 during the catalysis at 650°C for 240 hrs (Figure 1d). The preservation of catalytic activity, selectivities and H_2/CO molar ratio in Figure 1 confirms the high durability of the Rh_1/TiO_2 catalyst at the high temperature of 650°C, suggesting that the chemical and coordination environments of Rh atoms of this catalyst remained unchanged (Figure 1), which is further supported by in-situ and operando characterizations of 0.037%Rh/TiO_2 under the catalytic condition described below.

Chemical and coordination environment of Rh atoms of single-atom catalyst

The chemical and coordination environments of Rh atoms of 0.037wt%Rh/TiO_2 at the atomic scale were investigated through in-situ XANES and EXAFS studies. 20 mg of 0.037wt%Rh/TiO_2 (Catalyst #1) was loaded into the XAS reactor (XANES and EXAFS); a mixture of 10 ml/min 10% CH_4 and 10 ml/min 5% O_2 was introduced; thus, the gas hourly space

velocity (GHSV) in the XAS reactor of in-situ XAS studies at the beamline end-station was the same as that of catalytic measurements performed at our catalysis lab. The catalyst was heated to 650°C in the flow of the aforementioned reactant mixture. High activities and selectivity of the catalyst during the in-situ XAS studies at 650°C were confirmed through analysis with an on-line mass spectrometer analyzing the composition of gas received through a glass capillary installed on the outlet of the XAS reactor. During the in-situ studies, the generated fluorescence due to absorption of Rh K-edge was collected when the catalyst was in the mixture of 10% CH_4 and 5% O_2 upon catalysis at 650°C for 4 hrs. The Rh K-edge of Rh_1/TiO_2 (Catalyst #1) at 23231.0 eV (red line in Figure 2a) is close to that of Rh_2O_3 nanoparticles supported on Al_2O_3 (blue line in Figure 2a),[48] suggesting that Rh atoms of 0.037%Rh/TiO_2 are in an oxidized state. In addition, the observed energy spectrum of Rh K-edge of Rh_1/TiO_2 (red line in Figure 2a) is quite consistent with the energy spectrum of Rh K-edge (red line in Figure 3) theoretically simulated by using the structural model of single atom catalyst (Figure 2e) optimized in computational studies. The proposed structural model of 0.037%Rh/TiO_2 (Figure 2e) will be described and discussed in detail later in this article.

In *r*-space spectra of Rh K-edge of 0.037%Rh/TiO_2 (Figure 2b4), a main peak at 1.50 Å was observed and readily assigned to Rh-O bonds, consistent with Rh-O bonds of the reference sample, Rh_2O_3 nanoparticles supported on Al_2O_3 (Figure 2b2) and those reported in references.[48-50] Here 1.50 Å is the Rh-O distance in r-space spectrum before a phase correction. We note all the distances of EXAFS studies described in the following paragraphs are distances before phase correction except for a specific note. Compared to the observed Rh-O-Rh peak at 2.63Å from the reference sample (Rh_2O_3/Al_2O_3 in Figure 2b2), no such a Rh-O-Rh peak was observed in the spectra of 0.037wt%Rh/TiO_2 (Figure 2b4). In addition, the spectrum of Rh_1/TiO_2 (Figure

2b4) does not have the peak of Rh-Rh bonds of Rh foil observed at 2.35 Å (Figure 2b1). Thus, neither peak of Rh-O-Rh bond of Rh_2O_3 nanoparticles (2.63 Å) nor peak of Rh-Rh bond of metal Rh nanoparticles (2.30 Å) was observed in the r-space spectrum of 0.037 wt% Rh/TiO_2 (Figure 2b4). The difference in coordination environment among Rh_1/TiO_2, Rh_2O_3/Al_2O_3 and Rh foil was supported by wavelet transform (WT) of EXAFS data of references samples (Rh foil and Rh_2O_3/Al_2O_3) and the catalyst 0.037wt%Rh/TiO_2 (Figure 4). In Figure 4a, there is one major contour maximum observed in the WT plot of Rh foil at (11.6 $Å^{-1}$, 2.30 Å), which is attributed to the first shell Rh-Rh coordination pathway in foil sample. In the WT plot of Rh_2O_3 reference sample (Figure 4b), there is one major contour maximum at (7.7 $Å^{-1}$, 1.5 Å) for the first shell Rh-O coordination pathway, and another three minor contour bands at k =7.68 $Å^{-1}$, 10.5 $Å^{-1}$ and 13.4 $Å^{-1}$, which are assigned to the coordination with surrounding O and Rh atoms at R=2.5-2.6 Å in the second shell (Rh-O-Rh). However, in the WT plot of Rh_1/TiO_2 catalyst under POM at

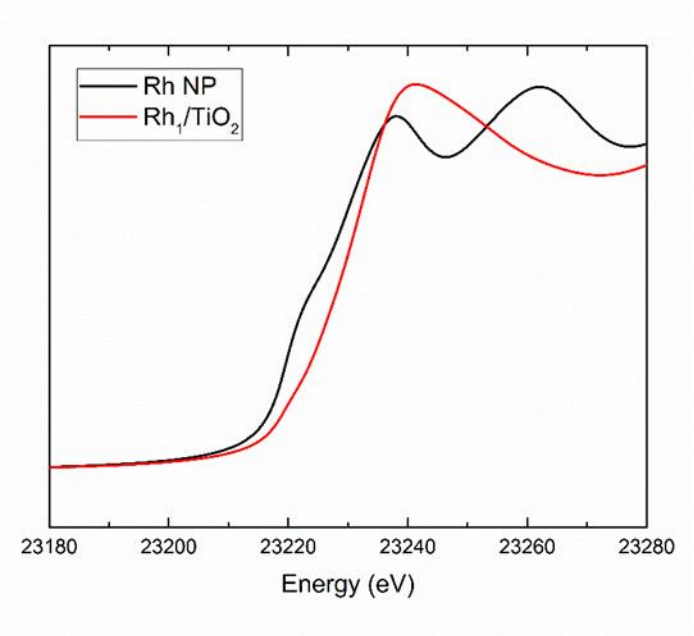

Figure 3. Theoretically simulated Rh K-edge energy spectra of Rh K-edge of single-atom catalyst Rh_1/TiO_2 and Rh nanoparticle. Red curve is the simulated spectrum of Rh_1 anchored on TiO_2 through the structural mode optimized with DFT (Figures 2e and 2f); black curve is the simulated spectrum of Rh nanoparticles consisting of 79 atoms (Rh_{79}) optimized with DFT (Figure S28b). The simulated spectra of Rh_1/TiO_2 and Rh nanoparticle are shown to be consistent with the observed spectra of Rh_1/TiO_2 (red curve in Figure 2a) and Rh foil (black curve in Figure 2a).

650ºC (Figure 4c), only one maximum at (7.6 $Å^{-1}$, 1.5 Å) is found for Rh-O coordination pathway, suggesting the lack of the second shell Rh-O-Rh on Rh_1/TiO_2. In addition, the contour maxima of Rh-Rh coordination which had been found in Rh foil and Rh_2O_3/Al_2O_3 are not observed in the WT plot of Rh_1/TiO_2, suggesting the lack of Rh-Rh coordination in the catalyst during POM. Figure 4 suggests that Rh atoms are singly dispersed in 0.037 wt% Rh/TiO_2 instead of forming Rh metal NPs or Rh_2O_3 NPs, further evidenced in the DRIFTS, CO chemisorption measurements, and AP-XPS studies to be discussed in the following paragraphs.

It could be argued that the peak of Rh-O-Ti of Rh_1/TiO_2 at 2.50 Å in Figure 2b4 could not be fully distinguished from the peak of Rh-Rh of Rh foil at 2.30 Å in Figure 2b1 due to the limited resolution of these r-space spectra, the following characterizations allow us to deduce that no Rh-Rh bonds contributed to this peak of Rh-O-Ti of Rh_1/TiO_2 at 2.50 Å in Figure 2b4. First, compared to the vibrational feature of CO adsorbed on Rh nanoparticles at 1872 cm^{-1} and 2060 cm^{-1} in the spectra of Diffuse Reflectance Infrared Fourier Transform Spectroscopy (DRIFTS) (Figure S10), the lack of the two peaks in the DRIFTS spectrum of the used Rh_1/TiO_2 (Figure 5) suggests that no Rh nanoparticles formed on surface of 0.037 wt% Rh/TiO_2 during catalysis at 650ºC since 1872 cm^{-1} and 2060 cm^{-1} are attributed to stretching of CO molecules adsorbed on surface of Rh metal nanoparticles (Figure S10) or the Rh single crystal.[51] The detailed pretreatment and collection of data of DRIFT spectra were described in Section 5 in SI. Peaks at 2090 cm^{-1} and 2022 cm^{-1} in the DRIFTS spectrum of Rh_1/TiO_2 in Figure 5 are assigned to asymmetric and symmetric stretching of C≡O of two CO molecules bound to a single Rh atom; this binding configuration is called geminal-dicarbonyl binding configuration in which two CO molecules are simultaneously bound to a metal atom. The vibrational signature in Figure 5 is very similar to that of single-atom catalysts reported in literature.[8,9] For Rh nanoparticles, such a geminal-dicarbonyl binding configuration should be a quite minor or even not present since Rh atoms on the surface of a Rh nanoparticle are continuously packed. Thus,

DRIFT studies suggests that no Rh NPs were formed on TiO_2 of 0.037wt%Rh/TiO_2 during catalysis at 650°C. Secondly, the measurement of the dispersion of Rh atoms of 0.037%Rh/TiO_2 by CO chemisorption showed that >97.5% of Rh atoms of the used 0.037%Rh/TiO_2 are singly dispersed on TiO_2; this further suggests that the fraction of Rh atoms of 0.037%Rh/TiO_2 catalyst that could potentially form Rh nanoparticles is lower than 2.5%. The single dispersion of Rh atoms on surface of 0.037%Rh/TiO_2 catalyst is suggested from CO chemisorption measurement, the vibrational signature of CO chemisorbed on 0.037 wt% Rh/TiO_2 and in-situ EXAFS studies. It is further supported with the lack of Rh nanoparticles on the used catalyst (Figures 2g and 2h) and the observation of singly dispersed Rh atoms (Figure 2i).

The peak at 2.50 Å in *r*-space of Rh K-edge of 0.037wt% Rh/TiO_2 (Figure 2b4 or Figure 2c) was fitted to Rh-O-Ti. Figure 2c presents the fitted *r*-space spectrum (in red) which matches the

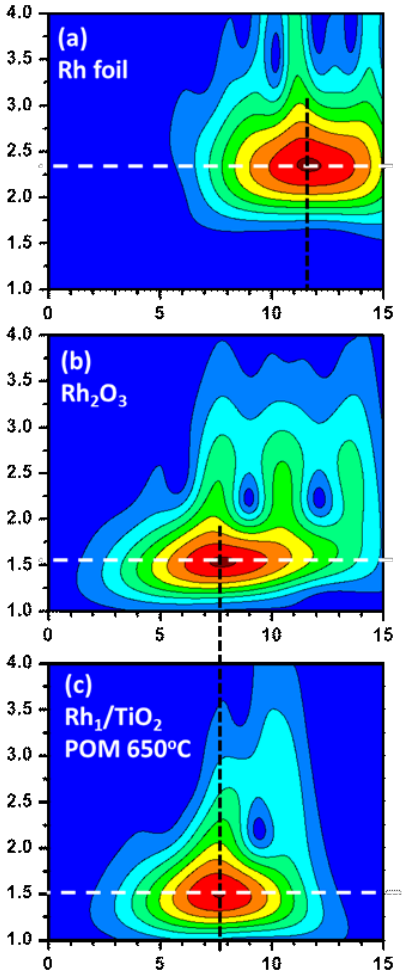

Figure 4. Wavelet transformation of EXAFS data of reference samples Rh foil (a), Rh_2O_3/Al_2O_3 nanoparticles (b), and the catalyst 0.037wt%Rh/TiO_2 (Rh_1/TiO_2) (c). Wavelet transformation parameters: HAMA Fortran package, k weight 2, Morlet function, kappa=5, and sigma=1.

experimental spectrum (in black) very well. The fitting parameters are listed in Figure 2d. This fitting shows (1) O and Ti atoms are in the first and second shells of Rh_1 atom of 0.037wt% Rh/TiO_2 under the catalytic condition at 650°C, respectively, (2) the coordination number of oxygen atoms in the closest shell of Rh_1 atom is about 5.76±0.69, and (3) the coordination number of Ti atoms in the second shell to Rh_1 is about 3.82. The average coordination number of oxygen atoms bonded to a singly dispersed Rh_1 atom is 5.76±0.69, suggesting that a Rh atom can substitute for either a Ti atom of the top layer (Figure S6a, Figure 2e or 2f) of TiO_2 or a Ti atom in subsurface or deeper layer of TiO_2 since the coordination number of O to a Ti atom in the top layer of Ti atom or in the subsurface of TiO_2 is 5 or 6, respectively. In fact, vast majority of Rh atoms of the used 0.037wt% Rh/TiO_2 substitute for *Ti atoms of the top layer in terms of the surface of TiO_2* instead of *Ti atoms in subsurface* of TiO_2 of Rh_1/TiO_2 since the dispersion of Rh atoms on surface of the 0.037 wt% Rh/TiO_2 is 97.5% based on the CO chemisorption measurements (Section 2 in SI).

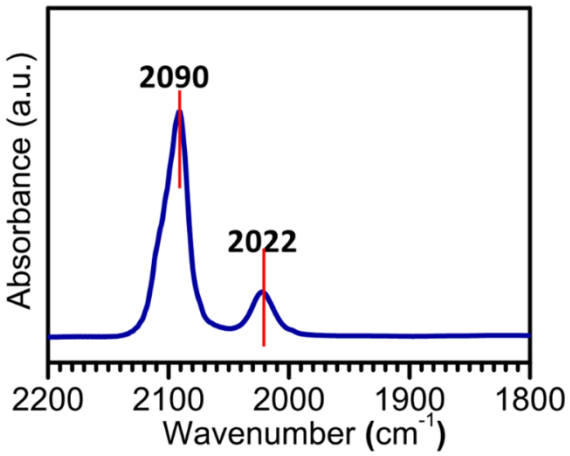

Figure 5. DRIFT studies of CO adsorbed on 0.037wt%Rh/TiO_2 (Rh_1/TiO_2).

As most users are usually only granted beam time of 1-3 days, continuously tracking catalyst structure with EXAFS in a period of 10 days was not realistic. The following in-situ XAS studies including XANES and EXAFS of Catalyst #2 was performed. To be specific, Catalyst #2 is 0.037wt%Rh/TiO_2 which has already been used for POM at 650 °C at catalysis lab before XAS studies. In-situ XANES and EXAFS studies of Catalyst #2 were performed under the same in-situ condition as Catalyst #1. Fittings the *r*-space spectrum

of Rh K-edge of Catalyst #2 (Figure S11b) shows that Rh atoms of Catalyst #2 were still singly dispersed. The fitting parameters of Figure S11b of Catalyst #2 listed in Figure S12 suggest the number of oxygen atoms coordinated with Rh_1 atom and bond length of Rh-O of the Catalyst #2 are similar to the Catalyst #1 (Figure 2d). The high similarity between the r-space spectra of catalyst #1 and catalyst #2 suggests the preservation of the coordination environment of Rh_1 atoms of Rh_1/TiO_2 during catalysis at 650°C. This structural preservation upon catalysis at 650°C well rationalizes the long durability of Rh_1/TiO_2 in terms of catalytic performance at 650°C (Figure 1).

The replacement of Ti cations in surface lattice of TiO_2 by Rh cations was supported by the observation of periodic peaks at 2.63 Å and 3.35 Å of Rh K-edge in r-space spectrum as

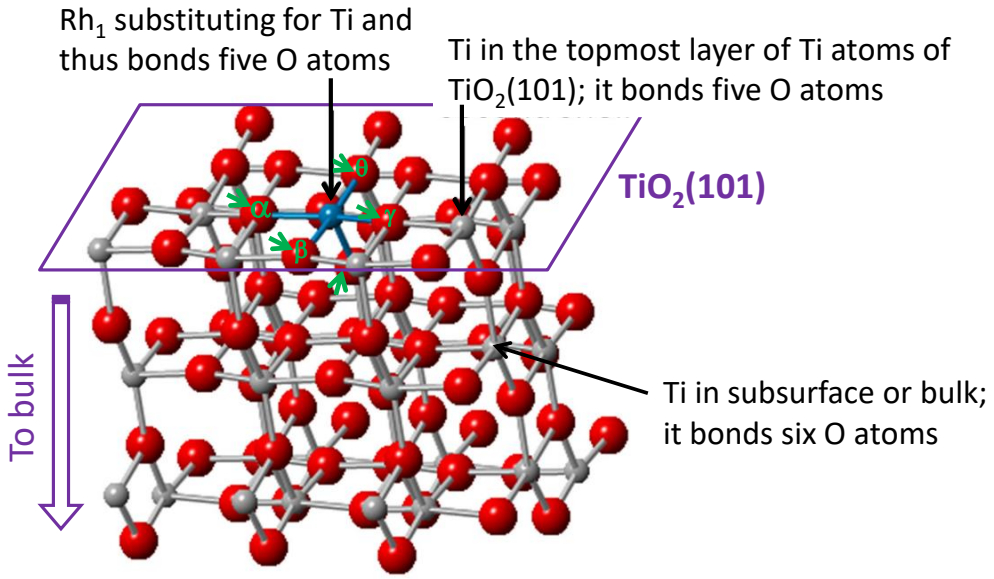

Figure 6. Structure of Rh_1/TiO_2 in which Rh_1 substituted Ti atom in surface lattice of TiO_2(101), optimized with DFT. Rh, O and Ti atoms are shown in blue, red, and gray, respectively. The five O atoms (directly bonding to Rh_1 on TiO_2(101) surface are marked with five green arrows. Compared to the first coordination shell of a Ti atom in subsurface or bulk, the first coordination shell of the Rh_1 is nearly saturated and thus it exhibits high stability. On the other hand, the unsaturation of the first coordination shell of the Rh_1 makes the Rh_1 reasonably strongly bound to C atoms of CH_4, CH_3 and CH_2 and thus makes Rh_1 highly active in transformation of CH_4 to CH_3, CH_3 to CH_2, and CH_2 to CH. The nearly saturated environment of Rh_1 makes the singly dispersed Rh_1 atom thermodynamically stable; thus, the Rh_1/TiO_2 exhibits long duration at 650°C for 240 hrs without decay of catalytic performance and high reusability.

marked with red dashed lines in Figure 2b4. These periodic peaks are in good agreement with the periodic peaks in r-space spectrum of Ti K-edge of Rh_1/TiO_2 (Figure 2b3) and those periodic peaks of bare TiO_2 (Figure S14a). Based on literature,[52,53] the appearance of the two peaks of Ti K- edge at 2.54 Å and 3.30 Å in Figure S14a was contributed from the periodic arrangement of Ti atoms (Ti-O-Ti^{α} and Ti-O-Ti^{β}) in the crystal lattice of pure TiO_2 (Figure 6). Compared to r-space spectrum of Ti K-edge of Ti atoms of TiO_2 (Figure 2b3), a very similar periodic pattern in *r*-space spectrum of Rh K-edge of Rh atoms of Rh_1/TiO_2 (Figure 2b4) was observed. This similarity suggests that these Rh_1 atoms substituted for Ti atoms in the surface lattice of TiO_2 (Figure S13f).

The chemical state of Rh atoms of Rh_1/TiO_2 during POM at 650°C was tracked with Ambient Pressure X-ray Photoelectron Spectroscopy (AP-XPS).[54] The formation of CO and H_2 on Rh_1/TiO_2 during AP-XPS studies was confirmed with an on-line mass spectrometer installed on AP-XPS, showing that the catalyst was active during the AP-XPS characterization at 650°C. The high binding energy of Rh $3d_{5/2}$ of Rh_1/TiO_2 at 310.2 eV (Figure 2j) suggests that Rh_1 atoms are in a cationic state during catalysis at 650°C. The high binding energy of Rh 3d peak of Rh_1/TiO_2 during catalysis observed experimentally is consistent with the electron transfer from d_{z^2} of Rh_1 atom to CH_4 proposed through computational studies.

As (101) is the dominant surface of this catalyst Rh_1/TiO_2 based on HAADF-STEM studies (Figures S13b-S13d), TiO_2 (101) was chosen as the surface to anchor the Rh_1 atom in the theoretical simulations of the surface structure of Rh_1/TiO_2. Based on the surface structure of TiO_2(101), Rh atom could be anchored through a substitution mode (Figure S6a) or three capping-on modes (Figures S6b-S6d). Computations of the energies of the four optimized structural modes in Figure S6 show that the substitution mode of Rh_1/TiO_2 is most thermodynamically favorable. In

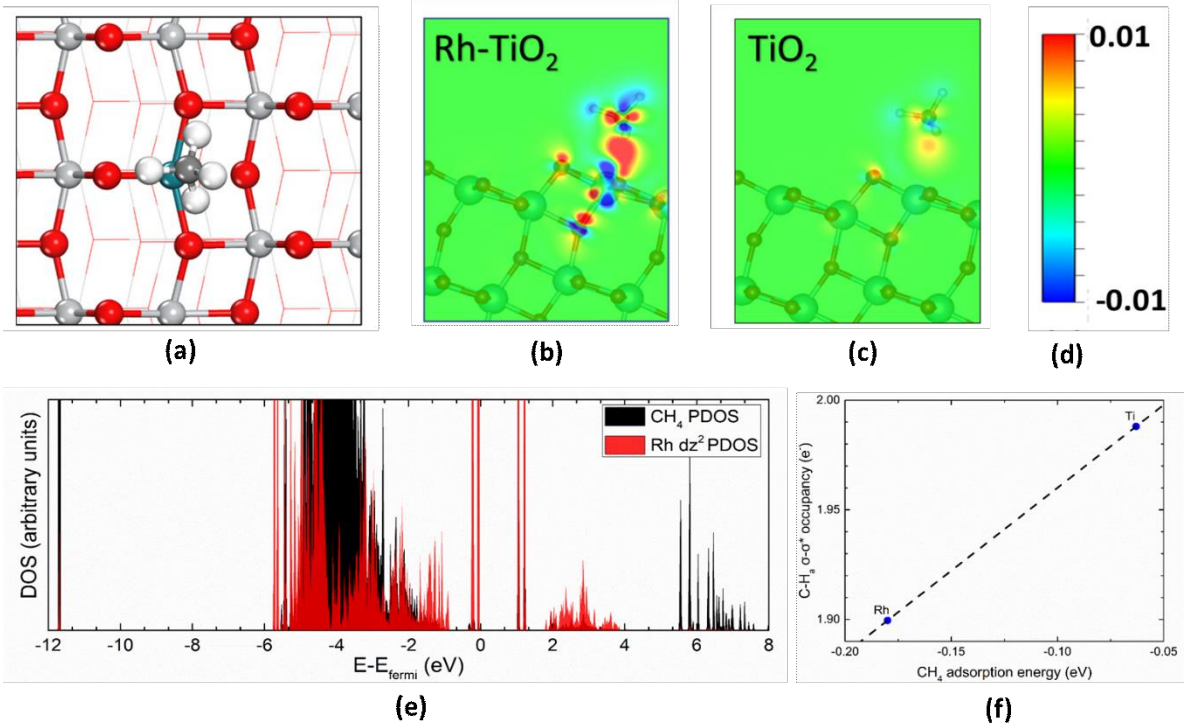

Figure 7. Geometrical and electron configurations and orbital coupling of CH_4 adsorbed on TiO_2 (101) generated from DFT calculations. (a) Top view of Rh_1/TiO_2 with chemisorbed CH_4. (b and c) Electron-density-difference plots of CH_4 on Rh atom of Rh_1/TiO_2 and CH_4 on Ti atom of bare TiO_2. (d) Color bar used to show relative electron density in (b) and (c), warmer color stands for higher electron density. (e) Partial density of states (PDOS) plots of the adsorbed CH_4 on Rh_1/TiO_2 obtained from DFT calculations; the projected states on dz^2 are shown for the Rh site. (f) Calculated linear correlation between the C-H_a σ-σ* occupancy and methane adsorption strength from periodic natural bond orbital (NBO) analysis.

this mode, an Rh atom substitutes for a Ti atom in the top layer of Ti atoms of the (101) surface of TiO_2 and thus each Rh_1 atom bonds with 5 oxygen atoms as shown in Figure 6, Figure 2e, or Figure S6a. The five O atoms bonding to Rh_1 on TiO_2(101) surface are marked with five green arrows in Figure 6. Here, Rh_1O_5 is used to refer the coordination environment of a Rh_1 atom of the catalyst during catalysis. The reasonability of the thermodynamically favorable substitution mode is supported by the consistency between the bond parameters of Rh-O obtained from the structural optimization in computational studies and these parameters generated from EXAFS experiments. Thus, the substitution structural mode in Figures

6 was used as the surface structure in the simulation of the catalytic mechanism of POM on the single-atom catalyst, Rh_1/TiO_2.

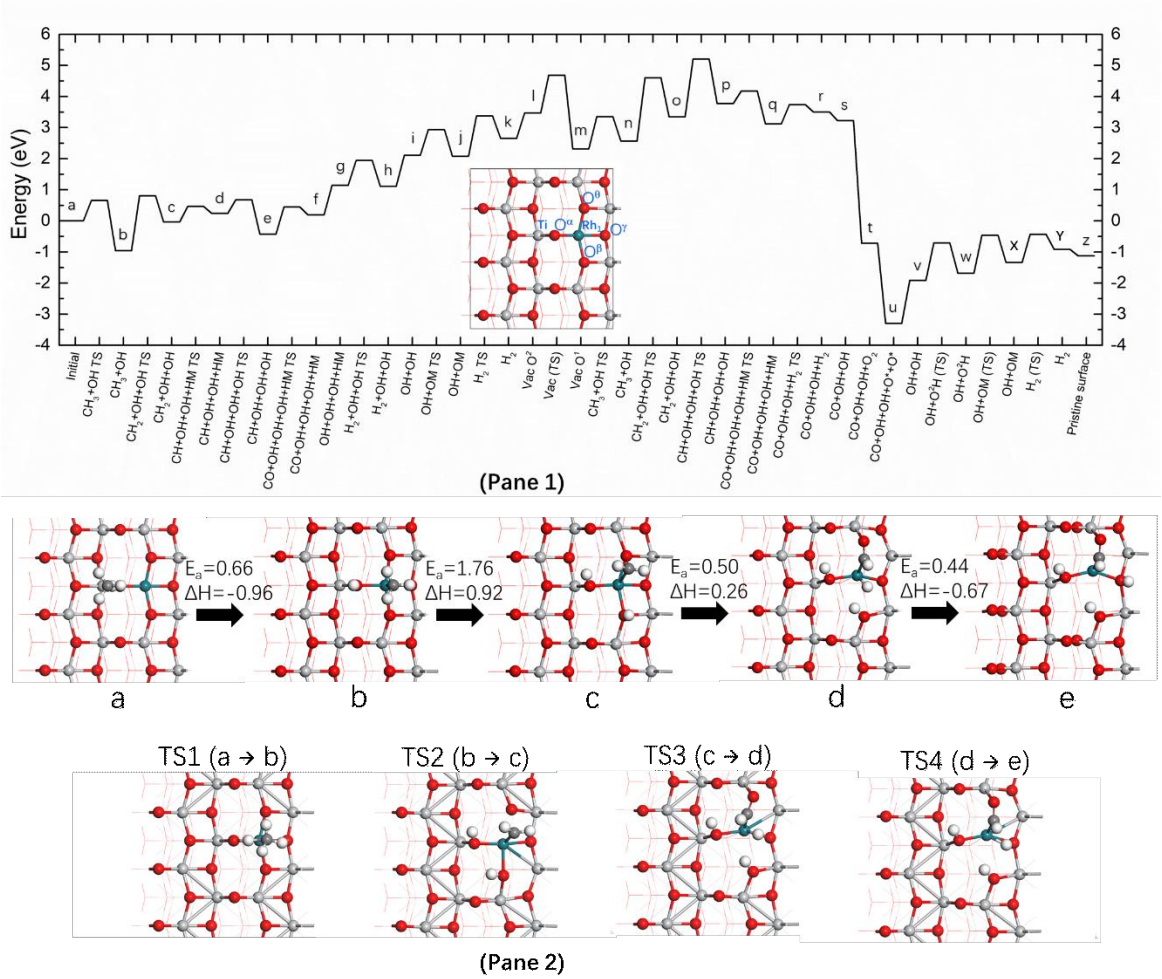

Figure 8. Enthalpy profiles of the compete pathway of POM consisting of 26 elementary steps on Rh_1/TiO_2 (Panel 1) and optimized structures of intermediates (*a*, *b*, *c*, *d*, and *e*) of activation of CH_4 on Rh_1O_5 to form CH_3 (*a*→*b*), CH_2 (*b*→*c*), and CH (*c*→*d*) and the transition state 1(*a*→*b*), transition state 2(*b*→*c*), transition state 3(*c*→*d*) and transition state 4(*d*→*e*) (Panel 2). Inset of panel 1 is the clean surface structure of Rh_1/TiO_2. All other intermediates and transition states are presented in Figures S18-S21.

To shed light on the POM mechanism, the adsorption and transformation of CH_4 on Rh_1/TiO_2

were explored through computational studies. Based on literature,[55-58] chemisorption of CH_4 typically involves the formation of an alkane σ complex. Charge transfer and orbital coupling between CH_4 and Rh_1 were studied with DFT. Figure 7a is the top view of the optimized

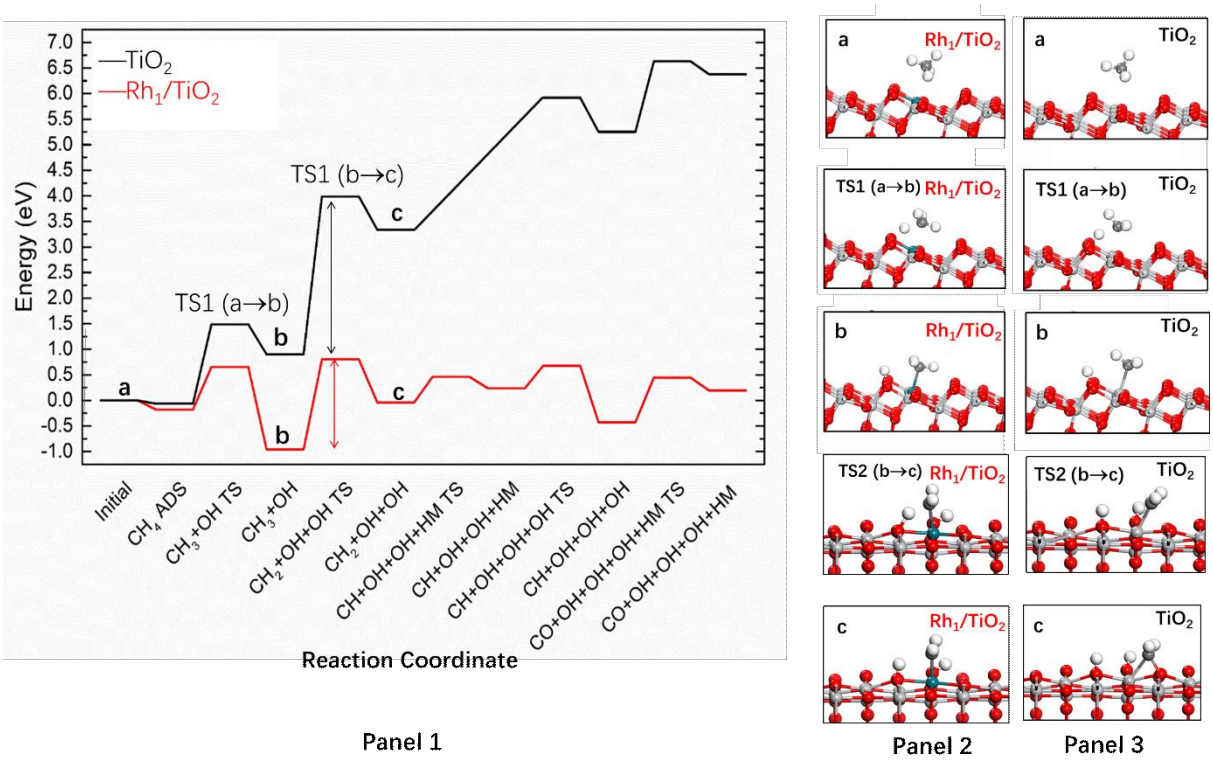

Figure 9. Energy profile of transformations of CH_4 to CH_3, CH_3 to CH_2, CH_2 to CH on Rh_1/TiO_2 and bare TiO_2. Obviously, the activation barriers on Ti cation of TiO_2(101) is much higher than that of Rh_1/TiO_2. In addition, compared to the Ti atom on surface of TiO_2(101), the binding energies of CH_3 of intermediate ***b*** on Rh_1 is increased by 3.4 eV; thus, the energy of intermediate ***b*** on Rh_1/TiO_2 is much lower than that on TiO_2 (see the energy level of intermediate ***b*** in Panel 1). The reasonably high binding energies of CH_3 to Rh_1 and H atom to its neighboring O atom in intermediate ***b*** on Rh_1/TiO_2 results in a lower activation barrier for dissociating CH_3 to CH_2 and H to form intermediate ***c*** on Rh_1/TiO_2 than that on TiO_2, based on the Brønsted–Evans–Polanyi relationship.

Rh_1/TiO_2 with a chemisorbed CH_4 molecule through binding C atom of CH_4 to Rh_1 atom. The calculated electron-density- difference plots of CH_4 on Rh atom of Rh_1/TiO_2 are shown in Figures 7b; electron density of Rh_1 of Rh_1/TiO_2 transferring to the C atom of CH_4 are mapped based on the color bar. Meanwhile, in the case of bare TiO_2, electron density of Ti of TiO_2 hardly transfer to CH_4 (Figure 7c). This specific difference can be found in the calculated Bader charges

(Figure S16). The substantial charge transfer from Rh_1 of Rh_1/TiO_2 to C atom of CH_4 is supported by the elongation of C-H from 1.096 Å of free CH_4 molecule to 1.115 Å of the chemisorbed CH_4 molecules on Rh_1 atom; however, the C-H bond distance of CH_4 adsorbed on bare TiO_2 (Figure S17) is 1.099 Å which is nearly the same as the free molecule.

To further understand the significance of Rh_1 in orbital coupling between CH_4 and Rh_1, partial density of states (PDOS) of CH_4 and Rh atom of Rh_1/TiO_2 with chemisorbed CH_4 were calculated. As shown in Figure 7e, molecular orbitals of CH_4 (black lines) mix most strongly with the d_{z^2} orbital of the substituting Rh_1 atom (red lines) since electron density of d_{z^2} orbital of Rh_1 can back donate to unoccupied orbital of the adsorbed CH_4 molecule. This back donation is consistent with the electron-density-difference plot in Figure 7b that shows a significant charge depletion around the Rh_1 atom and the corresponding charge enhancement around CH_4. The electron-density difference can be evaluated through the color code of Figure 7d. Moreover, the natural bond orbital (NBO) analysis in Figure 7f shows a lower C-H σ-σ* occupancy on Rh_1/TiO_2 than that on bare TiO_2, suggesting that Rh_1 of Rh_1/TiO_2 is quite favorable for activating the C-H bond. Thus, both electron density calculation and simulation of orbital coupling of CH_4 and Rh_1 show that Rh_1 is favorable for binding CH_4 and activating the C-H bond.

Molecular-level understanding of POM on Rh_1/TiO_2 at high temperature

Extensive computational studies were performed for optimizing intermediates and searching for transition states of POM performed on the optimized structure of Rh_1O_5/TiO_2 shown in Figure 6. These theoretical simulations proposed a complete catalytic cycle consisting of 26 elementary steps starting from chemisorption of reactants to form two CO and four H_2 molecules on Rh_1/TiO_2 ($2\ CH_4+O_2 \rightarrow 2CO+4H_2$). A complete energy profile of intermediates

and transition states of the entire pathway were plotted in panel 1 of Figure 8. All intermediates are listed in Figure S18 and Figure S19, respectively. Figures S20 and S21 present the structures of transition states of this complete reaction pathway of POM on Rh_1/TiO_2.

Notably, the activation of molecular O_2 on Rh_1/TiO_2 is distinctly different from that on an oxygen vacancy of a transition metal oxide. The activation was not performed at the beginning of the cycle as the surface at the beginning does not present oxygen vacancies and the adsorption of molecule O_2 on surface without oxygen vacancies is weak. Even if molecular O_2 is dissociated, the formed O atoms can thermodynamically favorably return to gas phase. Step ***t*** to ***u*** in Figure S19 is the activation of reactant O_2 through insertion of a molecular O_2 between Rh_1 atom and its nearest Ti atom in the intermediate **t**. Notably, this insertion step is kinetically barrierless and thermodynamically exothermic (panel 1 in Figure 6), suggesting a different path for activating molecular O_2 on Rh_1/TiO_2 in contrast to dissociation of O=O on oxygen vacancy on transition metal oxides. Different from the barrierless kinetics of molecular O_2 on this single atom catalyst Rh_1/TiO_2, kinetical barrier for activation of O_2 on Co_3O_4,[59] TiO_2,[60] CeO_2,[61] is in the range of about 0.5-2.0 eV, which varies at different faces and vacancies. Compared to the activation of O_2 on an oxygen vacancy of transition metal oxides, this distinctly different barrierless activation mechanism of O_2 on the site of Rh_1/TiO_2 demonstrated the significance of Rh_1 in the high activity of Rh_1/TiO_2 for POM. The presence of both undercoordinated Rh_1 atom and its nearly oxygen vacancies make dissociative adsorption of molecular O_2 significantly downhill with little or no barriers, thus stabilizing the dissociated O atoms even at high temperatures.

As can be seen from panel 2 of Figure 8, the Rh_1O_5 plays a crucial role in progressively activating CH_4 to form CH_3, CH_2 and CH before CH insets into Rh1-O^{θ} toward forming a CO molecule. The coupling between C-H of CH_4 and Rh_1-O^{α} of Rh_1O_5 (***a*** in panel 2 of Figure 8)

makes the first C-H bond broken, forming CH_3 on Rh_1 and H on O^{α} next to Rh_1 (***b*** in panel 2 of Figure 8). C-H of CH_3 couples with Rh_1-O^{β}, forming CH_2 on Rh_1 and H on O^{β} next to Rh_1 (***c***). In terms of transformation of CH_2 to CH, Rh_1-O^{β} is broken and then CH is inserted to Rh_1-O^{θ} (***d***) and thus forms Rh_1-C(H)-O^{θ}-Ti (***e*** in panel 2 in Figure 8). Upon -CH- is inserted, the H atom of CH transfers to Rh_1, forming Rh_1-C-O^{θ}-Ti (***f*** in Figure S18). C-H activations on Ti cation of bare TiO_2(101) were simulated; as shown in panel 1 (black line) and panel 3 in Figure 9, each of the three transformations ($CH_4 \rightarrow CH_3$, $CH_3 \rightarrow CH_2$, $CH_2 \rightarrow CH$) on Ti cation of bare TiO_2(101) experiences a much higher activation barrier than those on Rh_1 cation of Rh_1/TiO_2. It clearly shows that Rh_1 on TiO_2 plays a significant role in activation of CH_4, which is consistent with the significant charge transfer from Rh_1 of Rh_1/TiO_2 to C of CH_4 (Figure 7b) but negligible charge transfer from Ti of bare TiO_2 to C of CH_4 (Figure 7c). After transformation of CH_4 to CH whose C atom bonds with both O^{θ} and Rh_1, the C-H of CH breaks to lose its H atom to form a -CO^{θ} species whose C atom bridges on Rh_1 and Ti in ***e-f*** in Figure S18; then, both Rh_1-C(=O^{θ}) and (O^{θ}=)C-Ti bonds break to form the first CO molecule in the step of ***f-g***. Then, one O vacancy (O_{vac}) is created in ***g*** (Figure S18) due to the loss of O^{θ} as a part of the first product molecule CO. The coupling of two H atoms on Rh_1 forms the first H_2 molecule in ***h-i*** (Figure S18), so do the other two H atoms to form the second H_2 molecule in the step of ***k-l*** in Figure S18. Although the formation of H_2 is slightly uphill in terms of reaction enthalpy, the elevated temperatures under reaction conditions make it favorable for H_2(g) to form rather than stay dissociative adsorbed on the surface. Thus, H atom adsorbed on surface was a part of intermediate instead of a part of the active site for POM.

The C-H of the second CH_4 molecule is activated on Rh_1 with a reasonably low activation barrier due to the relatively low coordination number of O atoms to Rh_1 in the intermediate m

(***m-n*** in Figure S19), forming CH_3 bound to Rh_1 in ***n***; further C-H activation of CH_3 on Rh_1-O^{β} forms CH_2 whose C atom inserts between Rh_1 and O^{θ}, formingH_2C-O^{θ} and H_2C-Rh_1 in ***o***; the formed CH_2 loses a H atom to form CH whose C atom bonds with both O^{θ} and Rh_1 in ***p***; a CO-like species forms and its C atom bonds on Rh_1 after HC(=O) loses its H atom in ***q***; coupling of two H atoms forms the third H_2 molecule in ***r***; a molecular O_2 chemisorbs to bond with both Rh_1 and Ti in ***t***; then, CO species adsorbed on Rh_1 desorb as the second CO molecule (***u-v*** in Figure S19) in the catalytic cycle ($2CH_4+O_2 \rightarrow 2CO+4H_2$). Subsequently, the left two H atoms couple, forming the fourth H_2 molecule in ***v-y***. The last H_2 in the catalytic cycle desorbs in **y-z**, regenerating the initial surface where Rh_1 bonds with five O atoms (O^{α}, O^{β}, O^{γ}, O^{θ}, and one O in subsurface). The regenerated surface (***z***) in Figure S19 is ready for the second catalytic cycle. Through the 26 elementary steps, two CH_4 and one O_2 participated into the catalytic reaction on the Rh_1O_5 site anchored on TiO_2, forming two CO and four H_2 molecules.

As shown in Figures S18 and S19, most intermediates of the POM on Rh_1/TiO_2 directly bind to Rh_1 and its adjacent O or nearest Ti atom, further confirming the crucial role of the Rh_1 on TiO_2(101). Based on the energy profile of all intermediates and transition states in panel 1 in Figure 8, the three steps with highest activation barriers are ***b→c***, ***n→o***, and ***o→p*** with barriers of 1.76 eV, 2.30 eV and 1.86 eV, respectively. ***b→c*** is the activation of C-H of CH_3 of the first CH_4 on Rh_1 to form CH_2; ***n→o*** is the activation C-H of CH_3 of the second CH_4 on Rh_1 to form CH_2; ***o→p*** is the activation of CH_2 of the second CH_4 to form CH on Rh_1. Overall, the rate-determining step among the complete pathway of POM ($2CH_4+O_2 \rightarrow 2CO+4H_2$) on Rh_1/TiO_2 is the activation of C-H of CH_3 of the second CH_4 on Rh_1O_5 to form CH_2.

POM on Rh nanoparticles supported on TiO_2

In order to understand how the singly dispersed Rh_1 site could be different from its counterpart at high temperature, a surface consisting of closely packed Rh atoms was prepared for performing comparable studies on durability of catalyst under the same condition as Rh_1/TiO_2. Such a surface can be found on Rh nanoparticles supported on TiO_2, termed Rh NP/TiO_2. The precursor of Rh NP/TiO_2 was prepared through impregnation which is a method different from the deposition-precipitation method used in preparation of Rh_1/TiO_2. In the preparation of Rh NP/TiO_2, its precursor was reduced at 500ºC for 2 hrs and 650ºC for 2 hrs in 5% H_2 instead of calcination in air at 650ºC used in the preparation of Rh_1/TiO_2. Details of preparations of Rh NP/TiO_2 can be found in the section of Experimental Methods and Computational Approaches. This Rh NP/TiO_2 catalyst is active for POM in the temperature range of 300-650ºC (Figure S23). Statistical counting of over 500 Rh NPs of the used catalyst Rh NP/TiO_2 shows that the average size of the Rh NPs supported on TiO_2 after catalysis at 650ºC for 240 hr is approximately 3.0 nm (Figure S24). In the following sections, we use the labels Rh NP/TiO_2 and 6.3wt%Rh/TiO_2 interchangeably, referring to the same catalyst. Compared to 50 mg of 0.037wt%Rh/TiO_2 (Rh_1/TiO_2) at 450ºC, 500ºC, 550ºC or 650ºC (Figure S2), 50 mg of 6.3wt%Rh/TiO_2 exhibits similar conversion of CH_4 at these corresponding temperatures, respectively. However, they exhibit quite different catalytic selectivities for producing H_2 or CO (Figure S2 versus Figure S23).

Notably, the similar conversion of CH_4 exhibited by the two catalysts (50 mg Rh NP/TiO_2 *versus* 50 mg Rh_1/TiO_2) at a temperature such as 650ºC does not suggests any similarity in activity of their catalytic site. As TiO_2 is completely inert for oxidation of CH_4 in 300-700ºC (Figure S1), the conversions of CH_4 of 50 mg of 6.3wt%Rh/TiO_2 and 50 mg of 0.037wt%Rh/TiO_2

depend on the numbers of Rh atoms exposed on catalyst surface. For 50 mg of 0.037wt%Rh/TiO_2, the amount of *the exposed Rh atoms on the surface* to catalyze the conversion of CH_4 is 1.75×10^{-7} mol; however, for 50 mg of 6.3wt%Rh/TiO_2, the amount of *the exposed Rh atoms on the surface* to catalyze conversion of CH_4 is 1.07×10^{-5} mol. Calculations of the amounts of exposed Rh atoms on the catalyst surfaces were described in Section 6 of SI. The ratio of Rh atoms precipitated into the POM on 50 mg of 6.3wt%Rh/TiO_2 to that on 50 mg of 0.037wt%Rh/TiO_2 is about 61:1. Thus, although the conversions of CH_4 on the two catalysts are seemingly similar, the activities of each exposed Rh atoms of the two catalysts are in fact *distinctly* different. The difference in catalytic activity between the two catalysts was further confirmed by measuring the turn-over rates under the kinetics-controlled regime. As described in Section 4 of SI, the reaction rate of each catalyst was measured when the conversion of CH_4 is less than 10%. With the measured reaction rate at 650ºC under kinetics-controlled regime, the turn-over rates (TOR) of the two catalysts were calculated in Section 7 of SI. The TOR of H_2 on a Rh atom of single-atom catalyst 0.037wt%Rh/TiO_2 is 2428 H_2 molecules per minute but it is only 35.8 H_2 molecules per minute on an exposed Rh atom of Rh nanoparticle catalyst, 6.3wt%Rh/TiO_2. Details of the calculations of TORs using data of kinetics studies are described in Sections 7.2 and 7.3 in the SI. Demonstrably, the activity in terms of TOR of the single-atom catalyst Rh_1/TiO_2 at 650ºC is much higher than the Rh nanoparticle catalyst, Rh NP/TiO_2, at the same temperature.

Durability of single-atom catalyst Rh_1/TiO_2 at 650ºC

Other than the much higher activity of Rh_1/TiO_2 catalyst at 650ºC than Rh NP catalyst at this temperature, the high-temperature single-atom catalyst, Rh_1/TiO_2 exhibits a much longer durability in catalytic performance than the Rh NP/TiO_2 (Figure 1 *versus* Figure S27). It is

necessary to highlight that the comparison of the difference in durability of catalytic performance is for obtaining a fundamental understanding of the reason of the observed high-temperature durability of single-atom catalysts; and not for developing a commercial POM catalyst for production of syngas in industries.

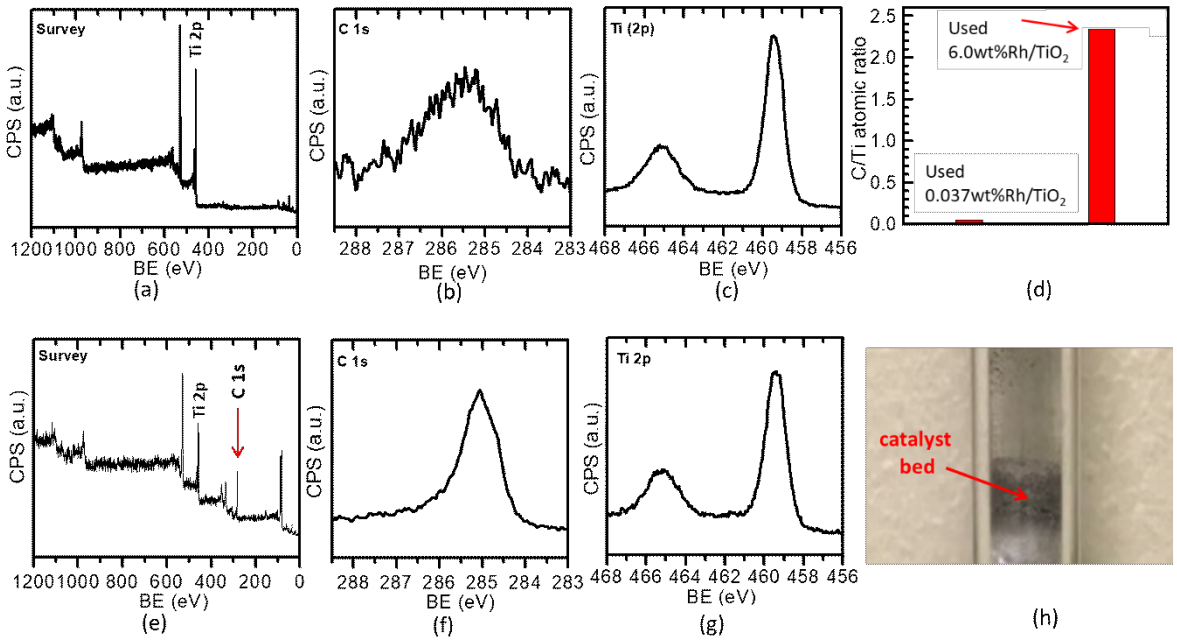

Figure 10. Formation of carbon layers on Rh NP/TiO_2 catalyst but not on Rh_1/TiO_2 based on XPS studies of 0.037wt%Rh/TiO_2 (Rh_1/TiO_2) and 6.3wt%Rh/TiO_2 (Rh NP/TiO_2) after catalysis at 650°C of 240 hrs. (a) Survey of the used 0.037wt%Rh/TiO_2 (Rh_1/TiO_2) catalyst; (b) C 1s spectrum of the used 0.037wt%Rh/TiO_2 (Rh_1/TiO_2) catalyst; (c) Ti 2p of the used 0.037wt%Rh/TiO_2 (Rh_1/TiO_2) catalyst; (d) C/Ti atomic ratio of the used 0.037wt%Rh/TiO_2 (Rh_1/TiO_2) catalyst and the used 6.3wt%Rh/TiO_2 (Rh NP/TiO_2) catalyst; (e) Survey of the used 6.3wt%Rh/TiO_2 (Rh NP/TiO_2) catalyst; (f) C 1s spectrum of the used 6.3wt%Rh/TiO_2 catalyst; (g) Ti 2p of the used 6.3wt%Rh/TiO_2 catalyst; (h) photo of the used 6.3wt%Rh/TiO_2 catalyst after catalysis at 650°C for 240 hours.

Compared to the nanoparticle catalyst (Rh NP/TiO_2), the single-atom catalyst (Rh_1/TiO_2) exhibits superior resistance to carbon formation. The continuously packed Rh atoms on surface of Rh nanoparticles of Rh NP/TiO_2 (Figure S28b) make CH_x (x=0-2) species adsorbed on two adjacent Rh atoms couple readily toward chain propagation leading to the formation of a coke

layer. As seen from XPS studies (Figures 10e, 10f and 10g), thick carbon layers were formed on the used Rh NP/TiO_2 after POM at 650°C for 240 hrs while negligible amounts of carbon were formed on Rh_1/TiO_2 after 240 hrs of POM at 650°C (Figure 10a, 10b and 10c). The atomic ratio of carbon atoms of surface carbon layers to all titanium atoms in surface region of used Rh NP/TiO_2 is about 2.5 (Figure 10d), suggesting the thickness of carbon is at least several atomic layers. It is much larger than that of Rh_1/TiO_2 used at 650°C for 240 hrs. The experimentally observed facile formation of carbon layers on Rh NPs is supported by the quite high adsorption energy of atomic carbon on Rh atoms of Rh nanoparticle surface uncovered in our computational studies (Figure S29b). Compared to the Rh atom on a Rh nanoparticle of 6.3wt%Rh/TiO_2, adsorption energy of atomic carbon on the singly dispersed Rh_1 atoms of 0.037wt%Rh/TiO_2 is lower by 2.8 eV (Figure S29); this significant difference in adsorption energy of carbon atom to Rh atoms of the two catalysts (Rh_1/TiO_2 versus Rh NP/TiO_2) results from the distinctly different coordination environment between Rh_1 of Rh_1/TiO_2 and Rh of Rh NP/TiO_2 (Figure S29). In terms of Rh_1/TiO_2, the singly dispersed Rh_1 atoms on TiO_2 does not provide opportunity for two CH_x (x=0-2) species adsorbed on spatially isolated Rh_1 atoms to couple since CH_x species on Rh_1/TiO_2 are spatially separated. Thus, Rh_1/TiO_2 exhibits high resistance to formation of coke at 650°C for a period of at least 240 hrs.

The high adsorption energy of atomic carbon on the surface of the metal Rh nanoparticle can rationalize the progressive decay of conversion of CH_4 to 60% at 105th hr and to nearly only 20% at 240th hr (Figure S27a). Along with the decay of catalytic activity, selectivities largely decreased to 86% for H_2 and 84% for CO at 105th hr and to 42% for H_2 and 29% for CO at 240th hr, respectively (Figures S27b and S27c). This significant decay of catalytic activity of 6.3 wt% Rh/TiO_2 is consistent with the observation of large amount of carbon formed on 6.3 wt%

Rh/TiO_2 after catalysis for 240 hrs at 650°C (Figure 10h).

The C/Ti atomic ratio of the 6.3 wt% Rh/TiO_2 catalyst used at 650°C for 240 hrs is about 45 times of that of the single atom catalyst Rh_1/TiO_2 catalyst used at the same temperature for the same amount of time (Figure 10d), rationalizing the significant decay of catalytic performance of 6.3wt%Rh/TiO_2 results from the formation of carbon layers on Rh nanoparticles which blocked the active sites. As reported in literature,[2,4,11-17] there are two types of carbons formed on POM catalysts including encapsulated carbon which blocks catalytic sites and thus obviously degrades catalytic performance, and whisker carbon which forms on a catalyst nanoparticle but sinks to one end of the catalyst nanoparticle and thus does not directly poison the catalyst surface but results in serious reactor clogging. As the reactor of 6.3wt%Rh/TiO_2 catalyst was not clogged after catalysis at 650°C for 240 hr, likely the encapsulated carbon instead of whisker carbon was formed on Rh NPs of 6.3wt%Rh/TiO_2. As these encapsulating carbon layers on the catalyst surface block the active sites, the catalytic activity clearly becomes degraded. The mechanism of deactivation of 6.3wt%Rh/TiO_2 is interesting and worth further studies. As the theme of this article is the molecular-level understanding of the high-temperature single-atoms catalytic chemistry of Rh_1/TiO_2 for POM, we leave the further studies of the deactivation of 6.3wt%Rh/TiO_2 in POM as a future task.

Conclusion

The high-temperature single-atom catalyst, Rh_1O_5/TiO_2 was prepared by substituting for Ti atoms of surface lattice with Rh atoms. The singly dispersed Rh_1O_5 clusters exhibit extraordinary catalytic performance of POM at 650°C including high activity, 98% selectivity for producing CO and 99% for H_2, long durability of 240 hrs, and high reusability over at least

20 cycles of catalysis. The single-atom site of this catalyst exhibits a turnover frequency of 2428 H_2 molecules per Rh_1 atom per minute at 650°C under kinetics-controlled regime. This extraordinary catalytic performance remains with no decay at 650°C for at least 240 hrs. Computational studies suggest that (1) activation barrier of the rate-determining step, dehydrogenation of CH_3 to CH_2 is greatly decreased while CH_3 and H bind to Rh_1 and O of Rh_1O_5 cluster of this catalyst, respectively, and (2) the long catalytic durability of Rh_1/TiO_2 at 650°C results from the unique coordination environment that Rh_1 atom on TiO_2 is in a nearly full coordination shell of oxygen atoms since Rh_1 coordinates with 5 oxygen atoms. Also benefited from the nearly saturated coordination of Rh_1 on TiO_2 surface, the adsorption energy of atomic carbon on Rh_1 is much lower than that on Rh atom with an obviously unsaturated shell on the surface of a Rh NP. The single dispersion of Rh_1 atoms on Rh_1/TiO_2 and the low binding energy of atomic carbon on Rh_1 of the Rh_1/TiO_2 effectively prevents the Rh_1/TiO_2 from forming carbon layers at high temperature, where the formation of carbon layers in POM on currently reported catalysts remains a common phenomenon. This study suggests an avenue for single-atom catalysis for significant chemical transformations at high temperatures.

Experimental Methods and Computational Approaches

Preparation of 0.037wt% Rh/TiO_2 (Rh_1/TiO_2). Single atom catalyst, termed 0.037wt% Rh/TiO_2 or Rh_1/TiO_2 was prepared with a modified deposition-precipitation method. Rhodium (III) nitrate hydrate, $Rh(NO_3)_3 \cdot 2H_2O$ (99.9%, Sigma-Aldrich) was used as the source of Rh cations for the preparation of the catalysts. A solution of Rh^{3+} with concentration of 2.84×10^{-3} mol/L was made for the following use. Crystallized TiO_2 nanoparticle with a size of 20-50 nm (99.9%, Sigma-Aldrich) was used as a TiO_2 support. The catalyst precursor of Rh_1/TiO_2

was prepared through a deposition precipitation method modified for the preparation of single-atom catalyst, Rh1/TiO_2. In a typical experiment, 500 mg TiO_2 was mixed with 50 mL deionized water through a vigorous stirring to form a white suspension. 3.0 mL $Rh(NO_3)_3 \cdot 2H_2O$ aqueous solution (2.84×10^{-3} mol/L) was introduced to the TiO_2 suspension through a precise injection with a syringe pump while the solution was vigorously stirred. The nominal loading is 0.20wt%. The new suspension was continuously stirred for 2 hours more to allow sufficient natural adsorption of metal ions. The pH value of the mixture was carefully adjusted to 9.5 by gradually introducing ammonium hydroxide solution, followed by vigorous stirring for 6 hours more in order to reach a complete equilibrium in solution. Then, the prepared solution was centrifuged and then dried at a 60^{o}C in overnight with a following calcination in Muffle furnace at 650^{o}C in air for 4 hours. The measured loading of Rh with ICP-AES is only 0.037±0.005wt%. Thus, either 0.037wt% Rh/TiO_2 or Rh_1/TiO_2 was used in the text for referring to this catalyst.

As described above, 0.037wt% Rh/TiO_2 was prepared through deposition-precipitation modified for this work. Based on the mechanism of the deposition-precipitation method, only a portion of cations were precipitated by OH^-. The portion of Rh^{3+} cations can be precipitated on TiO_2 depends on the pH of the solution. Higher pH allows a larger portion of Rh^{3+} cations to be precipitated. To make sure formation of singly dispersed Rh_1 on TiO_2 upon annealing at 650^{o}C in air instead of formation of Rh_2O_3 nanoparticles, the pH of the aqueous solution containing TiO_2 was controlled at 9.5. Based on ICP-AES measurements, the actual loading of Rh is 0.037wt%Rh. Thus, only about 18.5% of the Rh^{3+} cations dissolved in water were precipitated. The rest of the Rh^{3+} cations remained in solution and then was washed out upon centrifugation to separate the TiO_2 with precipitated Rh^{3+} in the form of $Rh(OH)_3$ from aqueous solution which contained the rest of Rh^{3+}. Certainly, the Rh^{3+} in aqueous solution can be readily reused by precipitation at high

pH to form $Rh(OH)_3$; a following calcination in air makes Rh_2O_3. A reduction of Rh_2O_3 in H_2 forms Rh metal nanoparticles. Thus, the preparation of Rh_1/TiO_2 does not waste the precursor of Rh^{3+}.

Preparation of 6.3wt%Rh/TiO_2 (RhNP/TiO_2). The 6.3wt%Rh/TiO_2 catalyst was prepared via impregnation method which is distinctly different from the modified deposition-precipitation method. 500 mg of TiO_2 powder was introduced to 0.50 ml aqueous solution of $Rh(NO_3)_3 \cdot 2H_2O$ which contains 33.36 mg Rh obtained from 85.18 mg of $Rh(NO_3)_3 \cdot 2H_2O$. The concentration of Rh would be 6.25wt% if all Rh atoms could be transferred to surface of TiO2 based on the calculation, $\frac{33.36\ mg\ Rh}{33.36\ mg\ Rh + 500\ mg\ TiO_2} = 6.25wt\%$. The impregnated sample was dried in a 60°C oven overnight and treated in flowing 5% H_2 in a tube furnace at 500°C for 2 hrs and then at 650°C for 4hrs. Based on ICP measurements, the concentration of Rh loaded on TiO2 is 6.3±0.3wt% which suggests most of the Rh atoms were transferred to TiO2. Upon the above procedure, Rh nanoparticles were formed on TiO2. Thus, either 6.3wt%Rh/TiO_2 or Rh NP/TiO_2 was used in the text to refer to this catalyst which is TiO_2 with loaded Rh NPs.

Compared to the preparation of single-atom catalysts described in the section of Experimental methods and computational approaches, the nanoparticle catalyst (6.3wt%Rh/TiO_2 or termed Rh NP/TiO_2) was prepared with the impregnation method instead of deposition precipitation used for Rh_1/TiO_2. The impregnated sample was dried in a 60°C oven in air overnight. Then, the dry catalyst precursor was treated in 5% H_2 at 500°C and 650°C instead of calcination in air at 650°C. In the preparation of Rh_1/TiO^2, pH of aqueous solution containing TiO_2 and Rh^{3+} cations was carefully controlled at pH=9.5. However, in the preparation of Rh NP/TiO_2, the solution containing $Rh(NO_3)_3$ solution and TiO_2 is at about 7.0. In the precipitation for preparation of Rh_1/TiO_2, only about 20% Rh^{3+} cations were precipitated; however, in the preparation of Rh

NP/TiO_2, all Rh^{3+} cations in solution were transferred to surface of TiO_2. Thus, the preparations of single-atom catalyst (Rh_1/TiO_2) and nanoparticle catalyst (Rh NP/TiO_2) were distinctly different.

NP-0.037wt% Rh/TiO_2 was prepared with the same preparation steps as 6.3wt% Rh NP/TiO_2: first impregnation of Rh^{3+} to TiO_2 and then drying at 120°C oven in air overnight and reduction at 650°C in 5% H_2 for 4 hrs in a tube furnace (the same protocol used to prepare 6.3wt% Rh NP/TiO_2). This preparation made Rh exist in the format of Rh nanoparticles supported on TiO_2. Thus, Rh of NP-0.037wt% Rh/TiO_2 exist in the format of Rh NPs, distinctly different from Rh1 atoms on 0.037wt% Rh/TiO_2. Unfortunately, the conversion of CH_4 in POM on 50 mg of NP-0.037wt% Rh/TiO_2 is actually much lower than detection limit of GC (<0.5% of CH_4).

DFT calculations. The density functional theory (DFT) calculations were performed with the Vienna ab initio Simulation Package (VASP).[2,3] The on-site Coulomb interaction was included with the DFT+U method by Dudarev et al.[4] in VASP using a Hubbard parameter U = 3 eV for the Ti atom, from the previous literature for TiO_2.[5,6] The Perdew-Burke-Ernzerhof (PBE)[5] functional form of generalized-gradient approximation (GGA) was used to describe electron exchange and correlation. In terms of unit cell, we used a 1×3 supercell of the stable (101) surface facet of bulk anatase TiO_2. Regarding to the distance between Rh atoms, the Rh atoms are separated by ~10 Å along each axis of the cell. About the Hubbard U correction, The Hubbard correction was applied for Ti d-orbitals of the model. As there have yet to be any studies investigating the optimal U value for Rh in TiO_2, we opted to not include a correction for Rh and we do not anticipate this will change the conclusions for the DFT calculations.

All calculations were performed with spin polarization. The projector-augmented wave method was used to describe the electron-core interaction[7,8] with a kinetic energy cutoff of 450

eV. The Brillouin zone was sampled with the Monkhorst-Pack scheme of a 3×2×1 k- point mesh.[8] Transition states (TS) were found with the nudged elastic band (NEB)[9] method using a force convergence criterion of 0.05 eV/Å. To calculate the occupancies of the molecular bonds of methane, the periodic natural bond orbital (NBO) analysis implemented by Schmidt et al. was used.[10]

Supporting Information

Size and morphology of 6.3wt%Rh/TiO_2; Chemisorption of CO on 0.037wt%Rh/TiO_2 and 6.3wt%Rh/TiO_2; Evaluation of catalytic performances of bare TiO_2, 0.037wt%Rh/TiO_2 and 6.3wt%Rh/TiO_2; Measurement of reaction rate under kinetics-controlled regime; Ex-Situ, In-Situ and Operando Characterizations; Calculations of the amount of Rh (in mol) *exposed to surface* of 50 mg of 0.037wt%Rh/TiO_2 and 50 mg of 6.3wt%Rh/TiO_2; Calculations of turn-over rates (TOR) of 0.037wt%Rh/TiO_2 (Rh_1/TiO_2) and 6.3wt%Rh/TiO_2 (Rh NP/TiO_2); Note on the difference in coordination environment of Rh atoms in 0.037wt%Rh/TiO_2 (Rh_1/TiO_2) and 6.3wt%Rh/TiO_2 (Rh NP/TiO_2); Note on AP-XPS studies.

Acknowledgements

This experimental part was supported by the NSF Career Award NSF-CHE-1462121 and Chemical Sciences, Geosciences and Biosciences Division, Office of Basic Energy Sciences, Office of Science, U.S. Department of Energy under Grant No. DE-SC0014561. The offer of beam time from the Innovation Research Center for Fuel Cells at The University of Electro-Communications and the assistance in data collection at Japan was highly appreciated. FT deeply thank Dr. M. Chi at ORNL for TEM studies of a part of the Rh_1/TiO_2 samples of this work and Dr. W. Hang at Iowa for assisting in DRIFT studies of some of the Rh_1/TiO_2 samples. FT highly appreciate collaborators at FZU for offering significant amount of machine

time for free access to their high-resolution TEM and other characterization instruments for extensive studies of samples before and after catalysis. Without the access to these characterization instruments of collaborators of FZU, it is impossible to finish this work at all. This work does not contain any classified information. All data and details of this work were/are published as the DOE and NSF projects acknowledged here were funded by chemistry division of NSF and office of science of DOE with the goal of pursuing publishable fundamental understanding of science of catalytic chemistry instead of any technique or knowhow with commercial values. None of these authors of this work thinks any part of this work could have any potential commercial value. None of these authors of this work thinks any part of this work could be combined or mingled with other work to generate classified information or commercial value.

References

1 Pena, M. A., Gomez, J. P. & Fierro, J. L. G. New catalytic routes for syngas and hydrogen production. *Applied Catalysis a-General* **144**, 7-57, doi:10.1016/0926-860x(96)00108-1 (1996).

2 York, A. P. E., Xiao, T. C. & Green, M. L. H. Brief overview of the partial oxidation of methane to synthesis gas. *Topics in Catalysis* **22**, 345-358, doi:10.1023/a:1023552709642 (2003).

3 Tsang, S. C., Claridge, J. B. & Green, M. L. H. RECENT ADVANCES IN THE CONVERSION OF METHANE TO SYNTHESIS GAS. *Catalysis Today* **23**, 3-15, doi:10.1016/0920-5861(94)00080-l (1995).

4 Vernon, P. D. F., Green, M. L. H., Cheetham, A. K. & Ashcroft, A. T. PARTIAL OXIDATION OF METHANE TO SYNTHESIS GAS. *Catalysis Letters* **6**, 181-186, doi:10.1007/bf00774718 (1990).

5 Byrne Jr, P. J., Gohr, E. J., Elizabeth, N. J. & Haslam, R. T. Recent Progress in Hydrogenation of Petroleum. *Industrial & Engineering Chemistry* **24**, 1129-1135, doi:10.1021/ie50274a009 (1932).

6 Nahar, G. & Dupont, V. Hydrogen production from simple alkanes and oxygenated hydrocarbons over ceria-zirconia supported catalysts: Review. *Renewable & Sustainable Energy Reviews* **32**, 777-796, doi:10.1016/j.rser.2013.12.040 (2014).

7 Amin, A. M., Croiset, E. & Epling, W. Review of methane catalytic cracking for hydrogen production. *International Journal of Hydrogen Energy* **36**, 2904-2935, doi:10.1016/j.ijhydene.2010.11.035 (2011).

8 Enger, B. C., Lodeng, R. & Holmen, A. A review of catalytic partial oxidation of methane to synthesis gas with emphasis on reaction mechanisms over transition metal catalysts. *Applied Catalysis a-General* **346**, 1-27, doi:10.1016/j.apcata.2008.05.018 (2008).

9 Liander, H. The utilisation of natural gases for the ammonia process *Transactions of the Faraday Society* **25**, 462-472, doi:10.1039/TF9292500462 (1929).

10 Prettre, M., Eichner, C. & Perrin, M. The catalytic oxidation of methane to carbon monoxide and hydrogen *Transactions of the Faraday Society* **42**, 335b-339, doi:10.1039/TF946420335B (1946).

11 Dissanayake, D., Rosynek, M. P., Kharas, K. C. C. & Lunsford, J. H. PARTIAL OXIDATION OF METHANE TO CARBON-MONOXIDE AND HYDROGEN OVER A NI/AL2O3 CATALYST. *Journal of Catalysis* **132**, 117-127, doi:10.1016/0021-9517(91)90252-y (1991).

12 Choudhary, V. R., Mamman, A. S. & Sansare, S. D. SELECTIVE OXIDATION OF METHANE TO CO AND H2 OVER NI/MGO AT LOW-TEMPERATURES. *Angewandte Chemie-International Edition in English* **31**, 1189-1190, doi:10.1002/anie.199211891 (1992).

13 Choudhary, V. R., Rajput, A. M. & Rane, V. H. LOW-TEMPERATURE CATALYTIC SELECTIVE PARTIAL OXIDATION OF METHANE TO CO AND H-2 OVER NI/YB2O3. *Journal of Physical Chemistry* **96**, 8686-8688, doi:10.1021/j100201a004 (1992).

14 Choudhary, V. R., Rajput, A. M. & Prabhakar, B. NONEQUILIBRIUM OXIDATIVE CONVERSION OF METHANE TO CO AND H-2 WITH HIGH SELECTIVITY AND PRODUCTIVITY OVER NI/AL2O3 AT LOW-TEMPERATURES. *Journal of Catalysis* **139**, 326-328, doi:10.1006/jcat.1993.1027 (1993).

15 Ruckenstein, E. & Hul, Y. H. Methane partial oxidation over NiO MgO solid solution catalysts. *Applied Catalysis a-General* **183**, 85-92, doi:10.1016/s0926-860x(99)00047-2 (1999).

16 Hu, Y. H. & Ruckenstein, E. Catalyst temperature oscillations during partial oxidation of methane. *Industrial & Engineering Chemistry Research* **37**, 2333-2335, doi:10.1021/ie980027f (1998).

17 Santos, A. *et al.* Oxidation of methane to synthesis gas in a fluidized bed reactor using MgO-based catalysts. *Journal of Catalysis* **158**, 83-91, doi:10.1006/jcat.1996.0008 (1996).

18 Lu, Y., Liu, Y. & Shen, S. K. Design of stable Ni catalysts for partial oxidation of methane to synthesis gas. *Journal of Catalysis* **177**, 386-388, doi:10.1006/jcat.1998.2051 (1998).

19 Liu, S. *et al.* Sustainable Ni catalyst for partial oxidation of CH4 to syngas at high temperature. *Studies in Surface Science and Catalysis* **130**, 3567-3572, doi:10.1016/S0167-2991(00)80576-5 (2000).

20 Choudhary, V. R., Uphade, B. S. & Mamman, A. S. Partial oxidation of methane to syngas with or

without simultaneous CO(2)and steam reforming reactions over NiAlPO4. *Microporous and Mesoporous Materials* **23**, 61-66, doi:10.1016/s1387-1811(98)00110-3 (1998).
21 Hayakawa, T. *et al.* A sustainable catalyst for the partial oxidation of methane to syngas: Ni/Ca1-xSrxTiO3, prepared in situ from perovskite precursors. *Angewandte Chemie-International Edition in English* **35**, 192-195, doi:10.1002/anie.199601921 (1996).
22 Basile, F. *et al.* Ni/Mg/Al anionic clay derived catalysts for the catalytic partial oxidation of methane - Residence time dependence of the reactivity features. *Journal of Catalysis* **173**, 247-256, doi:10.1006/jcat.1997.1942 (1998).
23 Peters, K., Rudolf, M. & Voetter, H. On the reaction pathway of methane reforming (germ.). *Brennstoff-Chemie* **36**, 257 (1955).
24 Ashcroft, A. T. *et al.* SELECTIVE OXIDATION OF METHANE TO SYNTHESIS GAS-USING TRANSITION-METAL CATALYSTS. *Nature* **344**, 319-321, doi:10.1038/344319a0 (1990).
25 Choudhary, V. R., Prabhakar, B., Rajput, A. M. & Mamman, A. S. Oxidative conversion of methane to CO and H-2 over Pt or Pd containing alkaline and rare earth oxide catalysts. *Fuel* **77**, 1477-1481, doi:10.1016/s0016-2361(98)00063-5 (1998).
26 York, A. P. E., Claridge, J. B., Brungs, A. J., Tsang, S. C. & Green, M. L. H. Molybdenum and tungsten carbides as catalysts for the conversion of methane to synthesis gas using stoichiometric feedstocks. *Chemical Communications*, 39-40, doi:10.1039/a605693h (1997).
27 York, A. *et al.* in *Studies in Surface Science and Catalysis* Vol. 110 711-720 (Elsevier, 1997).
28 Claridge, J. B. *et al.* New catalysts for the conversion of methane to synthesis gas: Molybdenum and tungsten carbide. *Journal of Catalysis* **180**, 85-100, doi:10.1006/jcat.1998.2260 (1998).
29 Qiao, B. *et al.* Single-atom catalysis of CO oxidation using Pt-1/FeOx. *Nature Chemistry* **3**, 634-641, doi:10.1038/nchem.1095 (2011).
30 Yang, X.-F. *et al.* Single-Atom Catalysts: A New Frontier in Heterogeneous Catalysis. *Accounts of Chemical Research* **46**, 1740-1748, doi:10.1021/ar300361m (2013).
31 Liang, S., Hao, C. & Shi, Y. The Power of Single-Atom Catalysis. *Chemcatchem* **7**, 2559-2567, doi:10.1002/cctc.201500363 (2015).
32 Lang, R. *et al.* Hydroformylation of Olefins by a Rhodium Single-Atom Catalyst with Activity Comparable to RhCl(PPh3)(3). *Angewandte Chemie-International Edition* **55**, 16054-16058, doi:10.1002/anie.201607885 (2016).
33 Sun, Q. *et al.* Zeolite-Encaged Single-Atom Rhodium Catalysts: Highly-Efficient Hydrogen Generation and Shape-Selective Tandem Hydrogenation of Nitroarenes. *Angewandte Chemie-International Edition* **58**, 18570-18576, doi:10.1002/anie.201912367 (2019).
34 Tang, Y. *et al.* Rh single atoms on TiO2 dynamically respond to reaction conditions by adapting their site. *Nature Communications* **10**, doi:10.1038/s41467-019-12461-6 (2019).
35 Wang, L. *et al.* Atomic-level insights in optimizing reaction paths for hydroformylation reaction over Rh/CoO single-atom catalyst. *Nature Communications* **7**, doi:10.1038/ncomms14036 (2016).
36 Guan, H. *et al.* Enhanced performance of Rh-1/TiO2 catalyst without methanation in water-gas shift reaction. *Aiche Journal* **63**, 2081-2088, doi:10.1002/aic.15585 (2017).
37 Han, B. *et al.* A highly active Rh-1/CeO2 single-atom catalyst for low-temperature CO oxidation. *Chemical Communications* **56**, 4870-4873, doi:10.1039/d0cc00230e (2020).
38 Ma, X.-L., Liu, J.-C., Xiao, H. & Li, J. Surface Single-Cluster Catalyst for N-2-to-NH3 Thermal Conversion. *Journal of the American Chemical Society* **140**, 46-49, doi:10.1021/jacs.7b10354 (2018).
39 Matsubu, J. C. *et al.* Adsorbate-mediated strong metal-support interactions in oxide-supported Rh catalysts. *Nature Chemistry* **9**, 120-127, doi:10.1038/nchem.2607 (2017).
40 Shan, J., Li, M., Allard, L. F., Lee, S. & Flytzani-Stephanopoulos, M. Mild oxidation of methane to methanol or acetic acid on supported isolated rhodium catalysts. *Nature* **551**, 605-+, doi:10.1038/nature24640 (2017).
41 Tang, Y. *et al.* Single rhodium atoms anchored in micropores for efficient transformation of methane under mild conditions. *Nature Communications* **9**, doi:10.1038/s41467-018-03235-7 (2018).
42 Nguyen, L. *et al.* Reduction of Nitric Oxide with Hydrogen on Catalysts of Singly Dispersed

Bimetallic Sites Pt1Com and Pd1Con. *ACS Catalysis* **6**, 840-850, doi:10.1021/acscatal.5b00842 (2016).
43 Leclerc, C. A., Redenius, J. M. & Schmidt, L. D. Fast lightoff of millisecond reactors. *Catalysis Letters* **79**, 39-44, doi:10.1023/a:1015348022952 (2002).
44 Schmidt, L. D. in *Studies in surface science and catalysis* Vol. 130 61-81 (Elsevier, 2000).
45 An, K. & Somorjai, G. A. Size and Shape Control of Metal Nanoparticles for Reaction Selectivity in Catalysis. *Chemcatchem* **4**, 1512-1524, doi:10.1002/cctc.201200229 (2012).
46 Borodko, Y., Ercius, P., Pushkarev, V., Thompson, C. & Somorjai, G. From Single Pt Atoms to Pt Nanocrystals: Photoreduction of Pt2+ Inside of a PAMAM Dendrimer. *Journal of Physical Chemistry Letters* **3**, 236-241, doi:10.1021/jz201599u (2012).
47 Borodko, Y. *et al.* From Single Atoms to Nanocrystals: Photoreduction of PtCl6 (2-) in Aqueous and Tetrahydrofuran Solutions of PVP. *Journal of Physical Chemistry C* **117**, 26667-26674, doi:10.1021/jp409960p (2013).
48 Glover, E. N. K., Ellington, S. G., Sankar, G. & Palgrave, R. G. The nature and effects of rhodium and antimony dopants on the electronic structure of TiO2: towards design of Z-scheme photocatalysts. *Journal of Materials Chemistry A* **4**, 6946-6954, doi:10.1039/c6ta00293e (2016).
49 Grunwaldt, J. D., Basini, L. & Clausen, B. S. In situ EXAFS study of Rh/Al2O3 catalysts for catalytic partial oxidation of methane. *Journal of Catalysis* **200**, 321-329, doi:10.1006/jcat.2001.3211 (2001).
50 Cavusoglu, G. *et al.* in *16th International Conference on X-Ray Absorption Fine Structure* Vol. 712 *Journal of Physics Conference Series* (2016).
51 Krenn, G., Bako, I. & Schennach, R. CO adsorption and CO and O coadsorption on Rh(111) studied by reflection absorption infrared spectroscopy and density functional theory. *Journal of Chemical Physics* **124**, doi:10.1063/1.2184308 (2006).
52 Bouchet, R., Weibel, A., Knauth, P., Mountjoy, G. & Chadwick, A. V. EXAFS study of dopant segregation (Zn, Nb) in nanocrystalline anatase (TiO2). *Chemistry of Materials* **15**, 4996-5002, doi:10.1021/cm034640n (2003).
53 Wu, Q., Zheng, Q. & van de Krol, R. Creating Oxygen Vacancies as a Novel Strategy To Form Tetrahedrally Coordinated Ti4+ in Fe/TiO2 Nanoparticles. *Journal of Physical Chemistry C* **116**, 7219-7226, doi:10.1021/jp212577g (2012).
54 Nguyen, L., Tao, F. F., Tang, Y., Doug, J. & Bao, X.-J. Understanding Catalyst Surfaces during Catalysis through Near Ambient Pressure X-ray Photoelectron Spectroscopy. *Chemical Reviews* **119**, 6822-6905, doi:10.1021/acs.chemrev.8b00114 (2019).
55 Hall, C. & Perutz, R. N. Transition metal alkane complexes. *Chemical Reviews* **96**, 3125-3146, doi:10.1021/cr9502615 (1996).
56 Weaver, J. F., Hakanoglu, C., Antony, A. & Asthagiri, A. Alkane activation on crystalline metal oxide surfaces. *Chemical Society Reviews* **43**, 7536-7547, doi:10.1039/c3cs60420a (2014).
57 Liang, Z., Li, T., Kim, M., Asthagiri, A. & Weaver, J. F. Low-temperature activation of methane on the IrO2(110) surface. *Science* **356**, 298-301, doi:10.1126/science.aam9147 (2017).
58 Saillard, J. Y. & Hoffmann, R. C-H AND H-H ACTIVATION IN TRANSITION-METAL COMPLEXES AND ON SURFACES. *Journal of the American Chemical Society* **106**, 2006-2026, doi:10.1021/ja00319a020 (1984).
59 Liu, J. *et al.* Tuning Catalytic Selectivity of Oxidative Catalysis through Deposition of Nonmetallic Atoms in Surface Lattice of Metal Oxide. *ACS Catalysis* **6**, 4218-4228, doi:10.1021/acscatal.5b02900 (2016).
60 Siemer, N. *et al.* Atomic-Scale Explanation of O-2 Activation at the Au-TiO2 Interface. *Journal of the American Chemical Society* **140**, 18082-18092, doi:10.1021/jacs.8b10929 (2018).
61 Brugnoli, L., Pedone, A., Menziani, M. C., Adamo, C. & Labat, F. O-2 Activation over Ag-Decorated CeO2(111) and TiO2(110) Surfaces: A Theoretical Comparative Investigation. *Journal of Physical Chemistry C* **124**, 25917-25930, doi:10.1021/acs.jpcc.0c09080 (2020).